High-Speed Optical Resolution Photoacoustic Microscopy With a MEMS Scanner: Novel and Simple Distortion Correction Method

Ryo Shintate (ryo.shintate.r4@dc.tohoku.ac.jp)
Tohoku University
Takuro Ishii
Tohoku University
Joongho Ahn
Pohang University of Science and Technology
Jin Young Kim
Pohang University of Science and Technology
Chulhong Kim
Pohang University of Science and Technology
Yoshifumi Saijo
Tohoku University

Research Article

Keywords: photoacoustic, microscopy, biomedical imaging, phantom, Leaf skeleton

Posted Date: November 22nd, 2021

DOI: https://doi.org/10.21203/rs.3.rs-1044038/v1

Abstract

Optical resolution photoacoustic microscopy (OR-PAM) is a remarkable biomedical imaging tool that can selectively visualize microtissues with optical-dependent high resolution. However, traditional OR-PAM using mechanical stages provides slow imaging speed, making biological interpretation of in-vivo tissue difficult. Here, we developed a high-speed OR-PAM using a recently commercialized MEMS mirror. This system (MEMS-OR-PAM) consisted of a 1-axis MEMS mirror and a mechanical stage. Furthermore, this study proposed a novel calibration method that quickly removes the spatial distortion caused by fast MEMS scanning. The proposed calibration method needs to run imaging sequence only once using a ruler target and it can easily correct distortions caused by both the scan geometry of the MEMS mirror and its nonlinear motion. The combination of the MEMS-OR-PAM and the distortion correction method was verified by three experiments.; 1) Leaf skeleton phantom imaging to test the distortion correction efficacy.; 2) Spatial resolution and depth of focus (DOF) measurement for the system performance.; 3) In-Vivo finger capillaries imaging to verify their biomedical use. The results showed that the combination could achieve a high-speed (32 sec in 2 mm×4 mm) and high-lateral resolution (~6 μm) imaging capability and precisely visualize the circulating structure of the finger capillaries.

Introduction

Photoacoustic microscopy (PAM) is a typical implementation of photoacoustic imaging (PAI) and is an innovative biomedical imaging technology that achieves high resolution, rich optical contrast, and superior penetration depth than optical imaging [1, 2, 3]. PAM systems employ a confocal structure of laser irradiation and ultrasound detection to generate and detect photoacoustic waves from an optical absorber in living tissues, and then perform volumetric data acquisition and image reconstruction of the subject. Furthermore, since the contrast of the reconstructed PA images depends on properties the optical absorber inside the tissue, PAM is capable of label-free anatomical and functional imaging by using the endogenous absorber such as oxy/deoxy-hemoglobin [4], melanin [5], and DNA/RNA [6]. Due to these unique advantages, PAM has been widely used in many clinical and preclinical studies such as oncology [5, 7], neuroscience [8, 9], histology [10, 11, 12, 13], dermatology [14] ophthalmology [15, 16], and cardiology [17].

Optical resolution photoacoustic microscopy (OR-PAM) is a PAM implementation to achieve higher spatial resolution [1, 18, 19]. It uses tightly focused laser irradiation much smaller than the acoustic reception focus. As a result, OR-PAM have achieved an optical-dependent high lateral resolution of 0.2-10 μm with a penetration depth of up to 1 mm [20,21,22,23.24], and, based on this high resolution, it has shown the potential to perform not only the clinical imaging of capillary and its metabolic activity but also the preclinical imaging of small animals such as mice [21, 25].

Despite of the prominent imaging capability, the conventional OR-PAM systems had a limited imaging speed because it employed a two-dimensional mechanical scanner equipped with stepping motor stages for the volumetric PA data acquisition [22, 23]. In particular, OR-PAM requires a large number of scan

points in order to reflect its high lateral resolution into the imaging quality, so the two-dimensional mechanical scanning takes a very long imaging time. In a previous paper, OR-PAM based on the mechanical stage had a 2D tomographic (B-mode) scan rate of 1 Hz/mm, and a 3D volumetric acquisition time of 7 minutes over a 1 × 1 mm^2 [23, 26, 27]. This long imaging time of conventional OR-PAM not only causes motion artifacts during PA imaging of living tissue, but also makes it difficult to the biological interpretation of the obtained PA images. Therefore, techniques that enable to increase imaging speed of OR-PAM have been in high demand.

In the earlier attempts of high-speed OR-PAM, a fast laser scanning method with a galvanometer scanner was used [28, 29, 30]. It performed fast laser scanning, and generated PA waves were detected with the fixed ultrasound transducer with the unfocused or weakly focused detection spot. However, this configuration provided a low SNR because the laser irradiation and ultrasound detection are not confocal. In addition, it had a very limited field of view (FOV) within the focal spot size of ultrasound detection.

On the other hand, the latest generation of fast OR-PAM employed a waterproof MEMS scanning mirror [31, 32, 33, 34, 35, 36, 37, 38, 39, 40]. In the fast PAM system, the coaxially and confocally adjusted laser irradiation beam and the ultrasound reception beam were scanned together by the MEMS mirror placed into the water. Hence, it achieved high-speed imaging while maintaining a high SNR and a better FOV. In addition, recently, this MEMS scanning mirror was commercialized [41, 42, 43]. This novel actuator has the potential to significantly overcome the problem on the imaging speed of conventional OR-PAM and enhances its impacts in medical and life sciences. Therefore, in this research, we aimed to develop a high-speed OR-PAM (MEMS-OR-PAM) system that utilizes the commercialized 1-Axis MEMS mirror.

When high-speed imaging with MEMS scanning mirror is performed as shown in Fig. 1, the scan geometry and the nonlinear scanning motion of the MEMS mirror have to be taken into account as it causes the distortion for obtained volumetric PA data and the reconstructed PA images [36, 44]. The nonlinear scanning motion of MEMS mirror is caused by the sinusoidal driving voltage when the mirror is operated at a high speed. Thus, it can be corrected by considering the sinusoidal driving characteristic into the scanning angle. Also, the scan geometry of MEMS mirror is a parabolic shape formed by the range of scan angle (θ_{scan}) and the working distance (WD) from the center of rotation of the mirror to the focal point of the confocal opto-acoustic beam. Therefore, it is considered as the polar coordinate, and the coordinate transformation can correct the image distortion caused by the geometry. However, to define the geometry accurately, it should be noted that prior knowledge of the following two parameters is required: 1) WD related to not only the focal length of the opto-acoustic beams but also the positional relationship of elements such as the MEMS mirror installed in the focused beam; and 2) θ_{scan} related to the amplitude of the MEMS driving voltage. The most typical method for knowing those parameters was doing many calibration measurements with the MEMS-OR-PAM system in various conditions [33, 35]. However, it was time-consuming and complicated to determine the accurate parameters, making the distortion correction difficult in practical imaging situations. Therefore, we needed a way to quickly estimate these two parameters (WD, θ_{scan}) and the geometry and easily correct the image distortion caused by the MEMS mirror without doing complicated experiments.

Therefore, in this research, in addition to the development of a novel MEMS-OR-PAM system, we proposed a novel method that easily corrects spatial distortion caused by high-speed scanning of a MEMS mirror by calibrating the system using a micron scaled ruler. In brief, the procedure consisted of five steps:

1) PA imaging in the desired imaging range while referring to the scale of the ruler;

2) Set virtual WD and θ_{scan} to virtually define the polar coordinate geometry for the acquired volumetric PA data;

3) Introduce the conversion equation to consider the nonlinear scan motion of MEMS mirror into the volumetric PA data and then perform the coordinate transformation;

4) Evaluate the effect of distortion correction from the reconstructed image; and

5) By repeating the steps 2) -4), determine the robust WD, θ_{scan}, and scan geometry for achieving the most distortion corrected image.

Not like the previous methods, the calibration method required to run imaging sequence only once before imaging the actual subjects (e.g., phantoms and living tissue). The effectiveness of the developed MEMS-OR-PAM and the calibration method was evaluated by the leaf skeleton phantom imaging, spatial resolution and depth of focus (DOF) measurements, and the finger capillaries imaging.

Materials And Methods

Single-Axis Waterproof MEMS (1A-WP-MEMS) Scanning Mirror

This study employed a single-axis waterproof MEMS scanning mirror (1A-WP-MEMS, OptichoMS-001, Opticho INC. Ltd., Republic of Korea). The fabrication method and specific specifications of the 1A-WP-MEMS mirror were described in a previous paper [34]. Briefly, the MEMS scanner consisted of two major modules, "movable structure layer" and "fixed block of electromagnets". The movable structure layer contained a PDMS layer, an acrylic frame, an aluminum mirror (reflection rate in water: 92% in laser / 84% in ultrasound), and neodymium magnets. The PDMS layer and acrylic frame firmly prevented the electromagnet of the fixed block from leaking electricity, thus forming a waterproof structure of the MEMS scanner. A magnetic field is generated when a driving voltage is applied to the electromagnets, and then an attractive and repulsive force is generated between the electromagnets and the neodymium magnet. This phenomenon causes a torque in the mirror on the movable layer, which rotates to scan the laser and ultrasound coaxial beams. The resonant frequency of the mirror used in this study was about 60 Hz (in the air) / 45 Hz (in water), and the maximum scan angle range was about 18 degrees.

Experimental Setup of MEMS-OR-PAM

Figure 2 shows a schematic diagram and photo images of the high-speed MEMS-OR-PAM system developed in this study. In this system, an Nd:YAG 532 nm laser (AWAVE532-1W-10K, Advanced Optowave; 10 ns pulse width; 10-100 kHz pulse repetition rate) was employed as a light source. The emitted laser beam was conveniently guided through the objective lens (OL1) to the PAM system by coupling to a multimode fiber (FC, FG010LDA, Thorlabs; 10 μm core diameter; 0.1 NA). The output laser beam from the fiber was shaped by a collimating lens (CL) and then split into two beams by a beam splitter (BS, FM01R; Thorlabs; >85% transmission rete). One beam (<15%) was reflected and guided to a photodetector (PD, PDA36A-EC, Thorlabs) as a trigger signal for data acquisition timing. The other beam (>85%), which was reshaped by the diameter of ~10 mm, is tightly focused by an achromatic doublet lens (OL2, AC254- 060-A, Thorlabs; 60 mm focal length; 0.2 NA). The focused laser beam was then combined coaxially and confocally with the acoustic reception beam by an opto-acoustic beam combiner (BC), an unfocused ultrasound transducer (UT, V214-BC-RM: 50 MHz center frequency: 80% -6 dB bandwidth, Olympus NDT), and an acoustic lens (AL, NT45-010, Edmund, USA; 0.25 NA). The BC consisted of a correction lens (NT67-147, Edmund, USA), an aluminum-coated prism (MRA10-G01, Thorlabs, USA), an uncoated prism (PS910, Thorlabs, USA) by joined all the components with optical adhesive (NOA61). This confocal structure was applied to maximize the SNRs of the PA signal. The opto-acoustic beam was reflected by the 1A-WP-MEMS mirror and irradiated onto the imaging target to generate the PA waves. The PA waves were detected by the ultrasound transducer and then amplified by two series-connected amplifiers (AMP, ZX60-3018G-S+ Mini-Circuit: 46dB total gain). A high-speed digitizer (ATS9350, Alazar Technologies: 500 MS/s sampling frequency) finally recorded the PA signals.

High-speed scanning was performed by the sinusoidal driving voltage applied to the MEMS mirror. The scanning sequence was performed by the combination of a high-speed MEMS scan in X-direction and a constant-velocity linear motion of the mechanical stage in Y-direction (see detailed scanning sequence in Supplementary Text A and Fig. S1).

Signal Processing and Image Reconstruction

The acquired volumetric PA signals were converted to analytic signal data by applying an IIR bandpass filter (5 - 120 MHz) and the Hilbert transform. After that, a 2D cross-sectional image was reconstructed by applying the Maximum Intensity Projection (MIP; thereafter called as C-mode) method to the volume PA envelopes [45]. In this study, a C-mode image shows the projected top-view (X-Y plane) of the imaging subject, while a B-mode image shows a slice of side views (X-Z or Y-Z planes) of the acquired three-dimensional image data. These image reconstructions were performed in real-time with LabVIEW software (National Instrument) and post-processed with MATLAB 2021b (MathWorks).

It is important to note that the volumetric PA data acquired and reconstructed at this stage involves spatial distortions caused by the fast MEMS scanning. The spatial distortion was corrected by a method described in the next section.

Correction method for the distortion derived by MEMS mirror scanning

As described in introduction, the volumetric PA data acquired with a high-speed MEMS-OR-PAM system is spatially distorted due to “the nonlinear scanning motion” and “the polar coordinate scan geometry” of the mirror [36]. The nonlinear scanning motion of the MEMS mirror is caused by the MEMS driving voltage applied as a sinusoidal wave for the high-speed operation. Here, when the driving voltage is applied as a triangular wave as shown in Fig. 3(a), the scanning property changes linearly with time (= θ_{linear}). In such a case, the volumetric PA data acquired at the timing of laser pulse repetition frequency (PRF) can be treated as a simple polar coordinate. However, the linear motion control has the drawback of slow scan speed, and it is not suitable for real-time imaging. On the other hand, when the MEMS driving voltage is applied as a sinusoidal wave as shown in Fig. 3(b), it can achieve high-speed operation as the actuator can move at around its resonant frequency. As a trade-off for imaging speed, the scanning angle transitions nonlinearly with time (=$\theta_{nonlinear}$). The nonlinear scanning angle characteristics when the MEMS mirror is driven by a sinusoidal wave can be expressed by the following equation [44],

$$\theta_{nonlinear} = \frac{\theta_{scan}}{2} sin \left(\frac{\theta_{linear}}{\theta_{scan}} \pi \right) \quad (1)$$

where $\theta_{nonlinear}$ is the nonlinear scanning angle characteristics, θ_{scan} is the range of scan angle in the imaging, and θ_{linear} is the linear scanning property assumed by PA acquisition timing with the laser PRF.

Regarding the polar coordinate geometry in the MEMS scan, it can be calculated from the working distance (WD) between the MEMS mirror and the focal position of the confocal opto-acoustic beam and the range of scan angle (θ_{scan}). In general, to obtain prior knowledge of WD and θ_{scan} is difficult as the relationship between θ_{scan} and the applied driving voltage amplitude can change by several conditions such as scan speed and mechanical property of MEMS mirror [33, 34, 36]. Also, WD cannot be simply determined because it is affected by not only the experimental focal length of the opto-acoustic beam but also the positional relationship of elements such as MEMS mirrors and beam combiners installed on the path of the focus beam [31, 32]. In order to estimate those parameters just before running imaging of the actual subject without any time-consuming or complex procedure, and easily correct its spatial distortion, a calibration method based on a single imaging of a ruler-target was proposed. The outline of the proposed method is shown in Fig. 4, and it consists of the following five steps.

1) PA imaging of the ruler (0.1mm Eyepiece Micrometer, Muhwa eCommerce Co. Ltd, Div. x: 0.1 mm; y: 0.1 mm) under the same imaging conditions as the subsequent phantom or tissue imaging. Here, we set the imaging area of X × Y=2 mm × 2 mm with 400 points × 400 points and laser PRF of 10 kHz. The depth position of the ruler is adjusted to the opto-acoustic focus. During the imaging, real-time image reconstruction (C-mode and B-mode image without distortion correction) was performed by LabVIEW, and the amplitude of the sinusoidal MEMS driving voltage was adjusted to include the ruler’s scale of the interest imaging region into the C-mode image. In this way, the optimum MEMS driving voltage amplitude for an interest imaging area could be easily determined.

2) **Linear Distortion Correction**: To define the polar coordinates geometry, WD and θ_{scan} are set virtually. WD can be selected from 4 mm to 10 mm., which is a rough value visually found. By the virtual WD, the scan range θ_{scan} can be calculated as follows,

$$\theta_{scan} = 2\tan^{-1}\left(\frac{X_{scale}/2}{WD}\right) = 2\tan^{-1}\left(\frac{1}{WD}\right) \quad (2)$$

where X_{scale} is the interest imaging range in the X-direction (2 mm). By setting WD and θ_{scan} virtually, the polar coordinate geometry can be defined. However, as mentioned earlier, the acquisition timing of the A-lines is based on the laser PRF, so the scanning angle property are assumed to be linear in this step. Therefore, if the cartesian coordinate transformation is performed with post processing in this step, the reconstructed image still distorted in both C-mode and B-mode images.

3) Nonlinear Distortion Correction: Applying Eq. (1) for transformation to the nonlinear scanning angle property. The resulting nonlinear polar coordinate geometry is transformed to cartesian coordinates to generate the distortion corrected reconstructed image.
4) For detecting the slight image distortion of B-mode image, extracting the intensity profile of the B-mode image and fitting it using the fact of the ruler target has a flat surface.
5) Repeating the steps 2)-4) while changing the virtual setting value of WD between 4 mm-10 mm. From the reconstructed C-mode and B-mode images and the flatness of the intensity profile of B-mode, we determine the best conditions of WD and θ_{scan} for the most distortion-corrected polar coordinate.
The polar coordinate obtained by the above method is also applied for image distortion correction in PA imaging of phantoms or living tissues under similar imaging conditions.

Imaging of a Leaf Skelton Phantom

To verify whether the proposed distortion correction method with a ruler and the obtained polar coordinates are also practical for imaging other measurement target, PA imaging of a black-stained leaf skeleton phantom was performed. The phantom was attached to the bottom of a dish filled with water and placed to the opto-acoustic beam focus of MEMS-OR-PAM. PA imaging was conducted in the region of X × Y=2 mm × 6 mm with 400 points × 1200 points. The laser PRF was 10 kHz and the emitted energy was ~100 nJ/pulse. After PA imaging, the obtained 3D volumetric data was applied the linear/nonlinear distortion correction to the X-direction (MEMS scan direction) by using the polar coordinate map obtained by the proposed method with a ruler. Then, the C-mode image and its Depth projection image were reconstructed using the volumetric PA data before and after distortion correction. The reconstructed PA images were compared with the phantom's photo image to verify the distortion correction's effectiveness.

Spatial Resolution and DOF Measurement

To verify whether the developed MEMS-OR-PAM with the distortion correction has a sufficient spatial resolution for microtissue imaging, we performed the lateral/axial resolution and DOF measurements.

For the lateral resolution measurement, PA imaging was performed with the USAF1951 target. The measurement range was X × Y = 2 mm × 2 mm (800 points × 800 points), the laser PRF was 10 kHz, and

the laser energy was <100 nJ/pulse. The USAF1951 has micro line patterns sputtered on the glass substrate. The lateral resolution conversion value was calculated from the smallest line patterns that can separate in the C-mode image after nonlinear distortion correction. In addition, to improve the reliability of the measurement, we also applied the Line Spread Function (LSF) method in this study. Specifically, the LSF method was performed by following three steps: 1) extract the edge spread function (ESF) of the line pattern in the C-mode image, 2) calculate the LSF, which is the differential waveform of the ESF, 3) measure the lateral resolution by calculating the full width at half maximum (FWHM) of the LSF.

For the axial resolution measurement, PA imaging was performed with a horizontally stretched carbon fiber with a diameter of 7 μm as shown in Fig. 5(a). The measurement range was X × Y = 2 mm × 1 mm (800 points × 400 points), and the laser PRF was 10 kHz, and the laser energy was <100 nJ/pulse. Obtained 3D volumetric data was applied nonlinear distortion correction, and then, C-mode image and B-mode image were reconstructed. The axial resolution was then calculated from the FWHM of the intensity profile in the B-mode image.

For the DOF measurement, a vertically tilted carbon fiber with a diameter of 7 μm was used as the imaging target as shown in Fig. 5(b). PA imaging of the target was performed in the range of X × Y = 2 mm × 10 mm (800 points × 4000 points), and the laser PRF was 10 kHz, the laser energy was <100 nJ/pulse. Obtained 3D volumetric data was applied nonlinear distortion correction, and then, the C-mode image and the Depth projection image were reconstructed. After that, the profiles of maximum PA Intensity and FWHM of the fiber along depth were created by associating both images. From these profiles, DOF was evaluated by two indicators: the depth range where 1) PA Intensity was half the peak, and 2) FWHM was expanded by $\sqrt{2}-1$ of the lateral resolution from the minimum FWHM. These indicators were used in the previous research [46] and the FWHM is associated with the theoretical evaluation [47].

As well as the measurements of the spatial resolution and the DOF, their theoretical values were calculated (described in Supplementary Text B and Fig. S2). As a result, the theoretical values of lateral and axial resolution and DOF were respectively found to be 7.0 μm, 32.6 μm, and 165.3 μm.

In-Vivo Microvascular Imaging of Human Finger

To verify the effectiveness of the MEMS-OR-PAM with the distortion correction for in-vivo imaging, PA imaging of the fingertips microvascular was performed. All the experimental procedures followed a protocol approved by the institutional review board (IRB) at Graduate School of Engineering, Tohoku University. In addition, all the methods were performed in accordance with the relevant guidelines and regulations. A healthy volunteer gave fully informed consent for imaging of his finger. In the imaging, the measurement range was X × Y = 2 mm × 4 mm (400 points × 800 points), the laser PRF was set to 20 kHz, and the pulse energy was 400 nJ/pulse. Here, since the laser PRF is twice higher than the previous in-vitro measurements, the driving frequency of the MEMS mirror was set twice as fast as before. Thus, the characteristics between the driving voltage amplitude and the corresponding scan range are slightly changed. Therefore, before the in-vivo PA imaging, calibration with a ruler was performed again to adjust

the MEMS driving voltage, and then microvascular imaging was performed. After the imaging, C-mode images without distortion correction and with nonlinear distortion correction were reconstructed, respectively. In addition, a B-mode image after the nonlinear distortion correction was reconstructed to investigate the penetration depth in the in-vivo imaging.

Before the imaging, the laser safety on the skin surface was calculated (Supplementary Text C and Fig. 3). As a result, in this experiment in which the focus position was set to the penetration depth of 300 μm where the capillary is present, the fluence was calculated to be 13.7 mJ/cm^2 on the skin surface, which met ANSI safety standards [48].

Results

Distortion Correction

Using the developed MEMS-OR-PAM system, the proposed distortion correction method using a ruler target was successfully validated. As described in Fig. 4, the calibration process was repeated by changing WD from 4 mm to 10 mm in 1 mm step to find the robust pair of WD and θ_{scan}. The observed distortions at each tested WD value can be seen in Supplementary Movie.

The PA intensity profiles extracted from the B-mode ruler images during the distortion correction process, PA intensity profiles after the linear distortion correction, the nonlinear distortion correction and its curve fitting result, were respectively shown in Figure 6(a), (b), and (c). In Fig. 6(a), the intensity profile after linear distortion correction, the nonlinear shape occurred in every WD because the nonlinear scan property is not considered. On the other hand, Fig. 6(b) shows the intensity profile after nonlinear distortion correction, and the nonlinear shape was removed, and only the curved shape of the profile was confirmed. The shape was close to horizontal when the WD was 6 mm to 8 mm. Fig. 6(c) shows the results of the curve fitting of the profile in Fig. 6(b), which could clarify the profiles and showed that the profile became the most horizontal and completely removed the distortion at WD = 7 mm. The scan range at WD=7 mm was calculated to be θ_{scan}=16.3 degrees from Eq. (2).

Figure 7 shows the results of the C-mode and B-mode images without/with distortion correction in [WD, θ_{scan}]=[7 mm, 16.3 degrees]. Figs. 7(a, d) show the image reconstruction result without distortion correction. In this result, since the image reconstruction was conducted from the volumetric PA data treated as a cartesian coordinate, the reconstructed image was distorted by both the scan geometry and the nonlinear motion of MEMS scanning. Figs. 7(b, e) show the results of linear distortion correction. The C-mode image in Fig. 7(b) was still distorted due to the nonlinear motion even after considering the polar coordinate geometry of MEMS scanning. Significantly in the C-mode image, the central part in the X-direction had compressed distortion, and the outer region had stretched distortion. This behavior was consistent with the nonlinear scanning property of the MEMS mirror shown in Fig. 3(a). In the B-mode image of Figs. 7(e), the distortion due to the geometry was removed compared to Fig. 7(d), but the distortion due to the nonlinear motion remained. Therefore, the linear distortion correction was not

sufficient in image reconstruction. On the other hand, Figs. 7(c, f) shows the nonlinear distortion correction results, and it clearly showed that the image distortion could be removed. In particular, in the C-mode image shown in Fig. 7(c), the ruler's scale was reproduced at equal intervals by removing the effect of the nonlinear motion of the MEMS scanning. Furthermore, in the B-mode image shown in Fig. 7(f), the distortion was also completely removed, and the centerline of the ruler's scale was reconstructed flat.

From these results, the proposed distortion correction method with a ruler suggested that it could readily determine the polar coordinate geometry of MEMS-OR-PAM and provide the distortion-free reconstructed images after the nonlinear distortion correction.

Leaf Skelton Phantom Imaging

Figure 8 shows the results of the Leaf Skelton Phantom, which photo image is Fig. 8(a). While Figs. 8(b, e, h) are images without any distortion correction, Figs. 8(c, f, i) and Figs. 8(d, g, j) are C-mode images and their enlarged C-mode images and the Depth projection images after applied linear and nonlinear distortion corrections.

For the C-mode images, the results in Figs. 8(b, c), which are the images without distortion correction and with linear distortion correction, showed that the phantom's structures are not reconstructed correctly and distorted compared to the optical image of Fig. 8(a). The corresponding enlarged C-mode images in Figs. 8(e, f) showed the distortions clearly in the X-direction due to the nonlinear MEMS scanning motion. On the other hand, in Figs. 8. (d, g), the C-mode image and its enlarged image with the nonlinear distortion correction, the distortions were removed, and the phantom's structure were correctly reconstructed compared to the photo image.

For the Depth projection image, the depth range of the reconstructed phantom was the narrowest in Fig. 8(j) with the nonlinear distortion correction, and it qualitatively showed that the distortion in the depth direction was removed. For quantitative evaluation of the distortion as the flatness, the maximum and minimum depth values and the depth width were calculated for the blue dotted square in Figs. 8(h-j), as shown in Table 1. As a result, the depth range with nonlinear distortion correction was smallest as 183 μm (Max: 519 μm / Min: 336 μm), which was 12.9% narrower than the result without distortion correction (210 μm) and 28.2% better than the result after linear distortion correction (255 μm). This result showed the effect of the distortion correction as the imaging flatness.

These qualitative and quantitative evaluations showed that the proposed distortion correction method with a ruler and the obtained nonlinear scan geometry works well for imaging other objects such as phantoms.

Spatial Resolution and DOF Measurement

Figure 9 shows the result of lateral resolution measurement using USAF1951. The lateral resolution calculation was performed for the C-mode image with nonlinear distortion correction shown in Fig. 9(b). From its enlarged C-mode image with a nonlinear distortion correction shown in Fig. 9(c), the smallest

line pattern that could be visibly separated in both the X and Y-direction was around Group 6 Element 3-4. Thus, the conversion value of lateral resolution was calculated as 5.5 μm - 6.2 μm. Also, in Figs. 9(d, e), the ESFs in the X and Y-direction were extracted, and the LSFs and its FWHMs were measured, respectively. As a result, the FWHMs were calculated as X: 5.6 μm / Y: 6.1 μm. Therefore, the experimental lateral resolution from the two methods was consistent, so the results were very reliable. Thus, the lateral resolution of the developed MEMS-OR-PAM was experimentally determined as ~6 μm, which was very close to the theoretical value (7.0 μm). This high lateral resolution showed the potential to sufficiently visualize microtissues such as human capillaries.

Figure 10 shows the results of axial resolution measurements using horizontally stretched carbon fibers. In Fig. 10 (c), the PA intensity profile in the depth direction along the red dotted line in Fig. 10 (b) was extracted, fitted by a Gaussian function, and then the FWHM of the fitted curve was utilized as the axial resolution of the MEMS-OR-PAM system. As a result, the experimental axial resolution was measured as 34.2 μm, which was in good agreement with the theoretical value (32.6 μm) calculated by the bandwidth of the ultrasound transducer.

Figure 11 shows the results of DOF measurement using the vertically tilted carbon fiber. In the images in Figs. 11(a, b), the fiber was vertically tilted along the Y-direction. Therefore, in the C-mode image of Fig. 11(a), the imaging contrast and sharpness were excellent in the central region of the Y-direction that the fiber was on the focus, while they became worse in the outside of the Y-direction where the focus was out from the fiber. In the Depth projection image of Fig. 11(b), the depth was calculated from the reception delay time of the PA intensity of Fig. 11(a) with intensity-based threshold cutting to project only the depth information from the fiber selectively. Based on these two images, the PA intensity and FWHM of the fiber along the depth direction were calculated as shown in Figs. 11(c, d), respectively. From the result of Fig. 11(c), the depth range at which the PA intensity is half of the peak was calculated as 370 μm. In Fig. 11(d), the FWHM of carbon fiber is calculated as 11 μm -16 μm with a depth range of 300 μm (150 μm - 450 μm). The minimum FWHM (11 μm) is slightly larger than the diameter of the fiber (7 μm) because the true profile of the fiber was convolved with the system PSF (point spread function), which is based on the experimental lateral resolution. The measured value of DOF was calculated as the depth range when the FWHM is 13.4 μm (11 μm + 2.4 μm), which is the value when the FWHM is expanded by $\sqrt{2}-1$ of the lateral resolution (6 μm) from the minimum FWHM. As a result, the measured DOF was calculated as 200 μm, slightly larger than the theoretical value (165.3 μm). Therefore, it was shown that the developed MEMS-OR-PAM has the potential to visualize microtissues while maintaining high contrast and lateral resolution within the long depth range.

In-Vivo Microvascular Imaging of Human Finger

Figure 12 shows the results of microvascular PA imaging of the fingertips. Here, the measurement time for the PA volumetric data acquisition was 32 seconds.

Figure 12(a) is a photo image of the fingertip, and the PA imaging was performed in the black dotted square. Fig. 12(b, c) are the C-mode images reconstructed without distortion correction and with nonlinear

distortion correction, respectively. From the two results, the nonlinear distortion correction of Fig. 12(c) successfully removed the image distortion compared with the C-mode image without distortion correction in Fig. 12(b).

In addition, Fig. 12(d) is an enlarged C-mode image of the white dotted square in Fig. 12(c), and the capillaries and their unique circulatory structure were visualized. Fig. 12(e) shows the PA intensity profile extracted from the white dotted line in Fig. 12(d), and the profiles distinguished the two blood vessels for the round trip in the circulatory structure. By applying the Gaussian fitting and calculating the FWHM of the intensity profile, the two diameters were found to be 26.4 μm and 22.3 μm, respectively. In addition, the FWHMs of the five circulatory structures (10 microvessels) in Fig. 12(d) were also calculated and averaged to obtain the accurate measurement values of the diameter. As a result, the average capillaries' diameter was 25.1 μm (SD 4.1 μm), and this result was within the range of 10 μm - 35 μm, which is the diameter of human capillaries previously reported [49, 50].

Figure 12(f) is the B-mode image along the blue dotted line in Fig. 12(c). From this result, microvessels mainly exist at a depth of 200 μm-300 μm from the skin surface, and as shown by the white arrow, the deepest microvessel was visualized at a depth of ~500 μm from the skin surface. Therefore, the in-vivo penetration depth of MEMS-OR-PAM was achieved at least 500 μm.

Discussion

Usefulness of the Proposed Distortion Correction Method

The distortion correction method by a ruler calibration proposed in this study could; 1) quickly adjust the MEMS driving voltage according to the interest imaging area (scan range) by referring to the ruler's microscale (takes only 10 minutes to the adjustment), 2) easily estimate the scan geometry and nonlinear scan motion of the MEMS scanning by post-processing, which previously requires complicated premeasurement to estimate, and 3) precisely correct the spatial distortion. As a result, the MEMS-OR-PAM using the distortion correction method could accurately visualize the capillary structure, as shown in Fig. 12 (b). Here, the remarkable point is that it has visualized even the circulatory structure of human capillaries, which is almost the first achievement on fast OR-PAM. Although a few studies previously visualized the structure by employing conventional mechanical scanning OR-PAM [51], its slow imaging speed made it difficult for biological interpretation. On the other hand, MEMS-OR-PAM provides fast imaging speed, but many studies were challenging to separately visualize the circulatory structure of human finger capillaries while they could clearly visualize the capillaries of nude mice [25, 40, 52]. It is because the human skin has strong optical scatterers such as melanin, which makes the lateral resolution degrade to blur the circulatory structure slightly, and thus, the additional image distortion leads to difficulty in visualizing such blurred structures separately. Therefore, for such near-clinical subjects, the distortion correction accuracy of the MEMS-OR-PAM is directly linked to the visualization performance of the circulation structure. Regarding that point, the proposed calibration method using a ruler performed precise distortion correction based on the accurate estimation of the MEMS scan geometry. That's why

the MEMS-OR-PAM system in this study has improved the separation performance of the circulatory structure of the capillaries. Such accurate PA imaging can promote the biological interpretation of microtissues such as capillaries and accurately grasp morphological changes such as structural abnormalities of capillaries [53]. The MEMS-OR-PAM, in this way, strengthens its biomedical application by combining it with the proposed distortion correction.

Furthermore, the advantage of the proposed distortion correction method is its flexibility in addition to its simplicity. Even if the measurement conditions are changed, we can quickly execute the distortion correction by calibrating the ruler again. For example, in the finger microvascular imaging shown in Fig. 12, since the laser PRF was changed to 20 kHz, higher than the phantom measurements (10 kHz), and the characteristics between the MEMS driving voltage amplitude and the scan angle were slightly changed. Even in such a case, if the MEMS scan range (2 mm) in imaging is the same, by performing only Step 1) of the ruler calibration method in Fig. 4, the drive voltage corresponding to the experimental conditions can be obtained, and the distortion correction can work again. Such flexibility of the proposed distortion correction may facilitate the medical application of MEMS-OR-PAM.

Imaging Speed and FOV of MEMS-OR-PAM

When performing in-vivo imaging with MEMS-OR-PAM, imaging speed and FOV are essential factors. In this research, in-vivo finger microvascular imaging was performed in a range of X × Y = 2 mm × 4 mm in 32 seconds (4 sec in 1 mm^2). It was 105 times faster than the typical mechanical scanning OR-PAM (7 min in 1 mm^2) [23]. This real-time imaging of MEMS-OR-PAM greatly prevents the occurrence of motion artifacts during bioimaging. As proof of this, capillary imaging using the developed MEMS-OR-PAM as shown in Fig. 12(c) clearly visualized the circulatory structure of capillaries, which should not be visible if even a small amount of motion artifacts occurs. However, if visualizing the more dynamic microvascular structure in the living body and the flowing of red blood cells inside the microvessels through it in real-time, it is necessary to have a wider FOV and faster imaging.

To improve the imaging speed, it is the most effective to employ a higher PRF of laser, assuming that the imaging range and the number of scan points are constant. However, it is a prerequisite that the PA waves generated for each laser pulse do not interfere with each other in the living body. Here, assuming that the speed of sound of living tissue is 1540 m/s and the maximum penetration depth is 500 μm, the propagation time of PA waves from the maximum depth to the tissue surface is 325 ns. In that case, the maximum effective PRF of the laser is 3 MHz. Therefore, there is no problem performing high-speed imaging in the PRF of 10-100 kHz, which is the operating range of the laser used in this study. If we use faster PRF than 100 kHz as the laser source, it is necessary to consider the influence of the pulse energy and SNR of PA signals, which are reduced by trade-off, and the limitation of the physical limitation operating speed of the MEMS mirror.

Regarding the improvement of imaging FOV, we have to consider each in X and Y-direction because the developed MEMS-OR-PAM employed the different scan method in each direction (X: MEMS scan, Y: Mechanical scan). The FOV in the Y-direction is determined by the operating length of the mechanical

stage. Here, the DOF measurement shown in Fig. 8 confirmed that the mechanical stage could operate in the range of 10 mm with no problem. In addition, the maximum operating length of the mechanical stage used in this study was defined as 20 mm, which was sufficient for in-vivo microtissue imaging in large FOV in the Y-direction. On the other hand, the FOV in the X-direction is determined by the MEMS mirror's physically limited scan angle (18 degrees). In this study, the scan angle for the imaging range of 2 mm was estimated as 16.3 degrees, which was close to the limitation. Therefore, the FOV in the X-direction is limited in a small area when using only the MEMS mirror. To overcome this limitation of FOV in the X-direction, combining the MEMS mirror and a mechanical stage is needed [35].

Medical Application of MEMS-OR-PAM

One of the practical medical applications of the MEMS-OR-PAM is to evaluate peripheral vascular disease caused by impaired microcirculation. For example, it has been suggested that thinning of capillaries contributes to hypertension [54, 55]. It can be a diagnostic index for subsequent diseases such as arteriosclerosis, myocardial infarction, and cerebral infarction. The developed MEMS-OR-PAM and the proposed distortion correction method have demonstrated the ability to selectively and clearly visualize the structure of capillaries. Thus, it can be a diagnostic technique for their medical needs.

Furthermore, in the future, we plan to employ the two-wavelength laser source to visualize the distribution of oxy/deoxy-hemoglobin in the capillary. It makes the developed MEMS-OR-PAM not only clearly visualize the circulating structure of capillaries but also monitor oxygen metabolism between capillaries and surrounding cells based on the spectral unmixing method [56] and possible to achieve functional imaging of microtissues.

Conclusions

In this paper, we reported the development of a high-speed OR-PAM system using a commercialized 1A-WP-MEMS scanning mirror and a novel calibration method that uses a micron-scale ruler for correcting the spatial distortion caused by the fast MEMS scanning. This novel method could easily and quickly find scan geometry and nonlinear scan motion of MEMS mirrors without complicated experimental measurements and could be applied for the distortion correction. The combination of the MEMS-OR-PAM and distortion correction was verified using artificial and biological subjects and the experimental results showed that the new fast OR-PAM system provides high-speed and high lateral-resolution imaging capabilities and precisely visualizes the circulating structure of capillaries in the human fingertip.

Declarations

Acknowledgment

This study was supported by ImPACT (Impulsing Paradigm Change through Disruptive Technologies) Program of Council for Science, Technology and Innovation (Cabinet Office, Government of Japan), Grants-in-Aid for Scientific Research (Scientific Research (B) 26282142, Challenging Exploratory Research

25560235), Grant-in-Aid for JSPS Fellows (21J13801) from the Japan Society for the Promotion of Science and Basic Science Research Program through the National Research Foundation of Korea (NRF) funded by the Ministry of Education (2020R1A6A1A03047902).

Competing interests

Chulhong Kim and Jin Young Kim have financial interests in Opticho, which, however, did not support this research.

Ryo Shintate, Takuro Ishii, Joongho Ahn, and Yoshifumi Saijo declare no competing interests.

References

1. Wang, L. V. & Yao, J. A practical guide to photoacoustic tomography in the life sciences. *Nat. Methods*, **13**, 627–638 (2016). https://doi.org/10.1038/nmeth.3925
2. Yao, J. & Wang, L. V. Sensitivity of photoacoustic microscopy. *Photoacoustics*, **2**, 87–101 (2014). https://doi.org/10.1016/j.pacs.2014.04.002
3. Wang, L. V. & Hu, S. Photoacoustic tomography: in vivo imaging from organelles to organs., **335**, 1458–1462 (2012). https://doi.org/10.1126/science.1216210
4. Hu, S., Maslov, K. & Wang, L. V. Second-generation optical-resolution photoacoustic microscopy with improved sensitivity and speed. *Opt. Lett*, **36**, 1134–1136 (2011). https://doi.org/10.1364/OL.36.001134
5. Wang, Y. *et al.* Fiber-laser-based photoacoustic microscopy and melanoma cell detection. *J. Biomed. Opt*, **16**, 011014 (2011). https://doi.org/10.1117/1.3525643
6. Yao, D. K., Maslov, K., Shung, K. K., Zhou, Q. & Wang, L. V. In vivo label-free photoacoustic microscopy of cell nuclei by excitation of DNA and RNA. *Opt. Lett*, **35**, 4139–4141 (2010). https://doi.org/10.1364/OL.35.004139
7. Kim, C. *et al.* In vivo molecular photoacoustic tomography of melanomas targeted by bioconjugated gold nanocages. *ACS Nano*, **4**, 4559–4564 (2010). https://pubs.acs.org/doi/pdf/10.1021/nn100736c
8. Nasiriavanaki, M. *et al.* High-resolution photoacoustic tomography of resting-state functional connectivity in the mouse brain. Proc. Natl. Acad. Sci. 111, 21-26(2014) https://doi.org/10.1073/pnas.1311868111
9. Hu, S. & Wang, L. V. Neurovascular photoacoustic tomography.*Front. Neuroenergetics***2** (2010) https://doi.org/10.3389/fnene.2010.00010
10. Zhang, C., Maslov, K. & Wang, L. V. Subwavelength-resolution label-free photoacoustic microscopy of optical absorption in vivo. *Opt. Lett*, **35**, 3195–3197 (2010). https://doi.org/10.1364/OL.35.003195
11. Zhang, C., Zhang, Y. S., Yao, D. K., Xia, Y. & Wang, L. V. Label-free photoacoustic microscopy of cytochromes. *J. Biomed. Opt*, **18**, 020504 (2013). https://doi.org/10.1117/1.JBO.18.2.020504

12. Wong, T. T. *et al.* Fast label-free multilayered histology-like imaging of human breast cancer by photoacoustic microscopy. *Sci. Adv*, **3**, e1602168 (2017). https://doi.org/10.1126/sciadv.1602168
13. BAIK, J. *et al.* Intraoperative Label-free Photoacoustic Histopathology of Clinical Specimens. *Laser Photonics Rev*, **15**, 2100124 (2021). https://doi.org/10.1002/lpor.202100124
14. Zhou, Y., Xing, W., Maslov, K. I., Cornelius, L. A. & Wang, L. V. Handheld photoacoustic microscopy to detect melanoma depth in vivo. *Opt. Lett*, **39**, 4731–4734 (2014). https://doi.org/10.1364/OL.39.004731
15. Jeon, S. *et al.* In vivo photoacoustic imaging of anterior ocular vasculature: a random sample consensus approach. *Sci. Rep*, **7**, 4318 (2017). https://doi.org/10.1038/s41598-017-04334-z
16. Silverman, R. H. *et al.* High-resolution photoacoustic imaging of ocular tissues. *Ultrasound Med. Biol*, **36**, 733–742 (2010). https://doi.org/10.1016/j.ultrasmedbio.2010.02.006
17. Zhang, C., Cheng, Y. J., Chen, J., Wickline, S. & Wang, L. V. Label-free photoacoustic microscopy of myocardial sheet architecture. *J. Biomed. Opt*, **17**, 0605061 (2012).
18. Park, J. *et al.* Quadruple Fusion Imaging via Transparent Ultrasound Transducer: Ultrasound, Photoacoustic, Optical Coherence, and Fluorescence Imaging. Proc. Natl. Acad. Sci. U. S. A. 118, e1920879118(2021) https://doi.org/10.1073/pnas.1920879118
19. Kim, H., Baik, J., Jeon, S., Kim, J. & Kim, C. PAExM: Label-free hyper-resolution photoacoustic expansion microscopy. *Opt. Lett*, **45**, 6755–6758 (2020). https://doi.org/10.1364/OL.404041
20. Maslov, K., Zhang, H. F., Hu, S. & Wang, L. V. Optical-resolution photoacoustic microscopy for in vivo imaging of single capillaries. *Opt Lett*, **33**, 929–931 (2008). https://doi.org/10.1364/OL.33.000929
21. Zhang, C. *et al.* Reflection-mode submicron-resolution in vivo photoacoustic microscopy. *J. Biomed. Opt*, **17**, 020501 (2012). https://doi.org/10.1117/1.JBO.17.2.020501
22. Hu, S., Maslov, K. & Wang, L. V. Noninvasive label-free imaging of microhemodynamics by optical-resolution photoacoustic microscopy. *Opt. Exp*, **17**, 7688–7693 (2009). https://doi.org/10.1364/OE.17.007688
23. Zhang, H. F., Maslov, K., Stoica, G. & Wang, L. V. Functional photoacoustic microscopy for high-resolution and noninvasive in vivo imaging. *Nat. Biotechnol*, **24**, 848–851 (2006). https://doi.org/10.1038/nbt1220
24. Shintate, R. *et al.* Development of optical resolution photoacoustic microscopy with sub-micron lateral resolution for visualization of cells and their structures. *Jpn. J. Appl. Phys*, **59**, SKKE11 (2020). https://doi.org/10.35848/1347-4065/ab840e
25. Kim, J. *et al.* Super-resolution Localization Photoacoustic Microscopy using Intrinsic Red Blood Cells as Contrast Absorbers. *Light: Sci. Appl*, **8**, 103 (2019). https://doi.org/10.1038/s41377-019-0220-4
26. Yao, J. & Wang, L. V. Photoacoustic Microscopy. *Laser Photonics Rev*, **7**, 758–778 (2013). https://doi.org/10.1002/lpor.201200060
27. Maslov, K., Stoica, G. & Wang, L. H. V. In vivo dark-field reflection-mode photoacoustic microscopy. *Opt. Lett*, **30**, 625–627 (2005). https://doi.org/10.1364/OL.30.000625

28. Xie, Z., Jiao, S., Zhang, H. F. & Puliafito, C. A. Laser-scanning optical-resolution photoacoustic microscopy. *Opt. Lett*, **34**, 1771–1773 (2009). https://doi.org/10.1364/OL.34.001771
29. Rao, B. *et al.* Real-time four-dimensional optical-resolution photoacoustic microscopy with Au nanoparticle-assisted subdiffraction-limit resolution. *Opt. Lett*, **36**, 1137–1139 (2011). https://doi.org/10.1364/OL.36.001137
30. Hajireza, P., Shi, W. & Zemp, R. J. Label-free in vivo fiber-based optical-resolution photoacoustic microscopy. *Opt. Lett*, **36**, 4107–4109 (2011). https://doi.org/10.1364/OL.36.004107
31. Kim, J. Y., Lee, C., Park, K., Lim, G. & Kim, C. Fast optical-resolution photoacoustic microscopy using a 2-axis water-proofing MEMS scanner. *Sci. Rep*, **5**, 7932 (2015). https://doi.org/10.1038/srep07932
32. Yao, J. *et al.* High-speed label-free functional photoacoustic microscopy of mouse brain in action. *Nat. methods*, **12**, 407–410 (2015). https://doi.org/10.1038/nmeth.3336
33. Kim, S. *et al.* Two-axis polydimethylsiloxane-based electromagnetic microelectromechanical system scanning mirror for optical coherence tomography. *J. Biomed. Opt*, **21**, 106001 (2016). https://doi.org/10.1117/1.JBO.21.10.106001
34. Kim, J., Lee, C., Park, K., Lim, G. & Kim, C. A PDMS-based 2-axis waterproof scanner for photoacoustic microscopy. *Sensors*, **15**, 9815–9826 (2015). https://doi.org/10.3390/s150509815
35. Baik, J. W. *et al.* Super Wide-field Photoacoustic Microscopy of Animals and Humans In Vivo. *IEEE Trans. Image Process*, **39**, 975–984 (2019). https://doi.org/10.1109/TMI.2019.2938518
36. Park, K. *et al.* Handheld photoacoustic microscopy probe. *Sci. Rep*, **7**, 13359 (2017). https://doi.org/10.1038/s41598-017-13224-3
37. Jeon, S., Kim, J., Lee, D., Woo, B. J. & Kim, C. Review on practical photoacoustic microscopy. *Photoacoustics*, **15**, 100141 (2019). https://doi.org/10.1016/j.pacs.2019.100141
38. Lee, C., Kim, J. Y. & Kim, C. Recent Progress on Photoacoustic Imaging Enhanced with Microelectromechanical Systems (MEMS) Technologies. *Micromachines*, **9**, 584 (2018).
39. Cho, S. *et al.* High-speed Photoacoustic Microscopy: A Review Dedicated on Light Sources. *Photoacoustics*, **24**, 100291 (2021). https://doi.org/10.1016/j.pacs.2021.100291
40. Ahn, J., Kim, J., Choi, W. & Kim, C. High-resolution Functional Photoacoustic Monitoring of Vascular Dynamics in Human Fingers. *Photoacoustics*, **23**, 100282 (2021). https://doi.org/10.1016/j.pacs.2021.100282
41. Moothanchery, M. *et al.* Optical resolution photoacoustic microscopy based on multimode fibers. *Biomed. Opt. Express*, **9**, 1190–1197 (2018). https://doi.org/10.1364/BOE.9.001190
42. Moothanchery, M. *et al.* High-speed simultaneous multiscale photoacoustic microscopy. *J. Biomed. Opt*, **24**, 086001 (2019). https://doi.org/10.1117/1.JBO.24.8.086001
43. Mai, T. T. *et al.* In Vivo Quantitative Vasculature Segmentation and Assessment for Photodynamic Therapy Process Monitoring Using Photoacoustic Microscopy. *Sensors*, **21**, 1776 (2021). https://doi.org/10.3390/s21051776

44. Cho, S., Baik, J., Managuli, R. & Kim, C. 3D PHOVIS: 3D photoacoustic visualization studio. *Photoacoustics*, **18**, 100168 (2020). https://doi.org/10.1016/j.pacs.2020.100168
45. Cody, D. D. AAPM/RSNA physics tutorial for residents: topics in CT. Image processing in CT., **22**, 1255–1268 (2002). https://doi.org/10.1148/radiographics.22.5.g02se041255
46. Yang, X., Song, X., Jiang, B. & Luo, Q. Multifocus optical-resolution photoacoustic microscope using ultrafast axial scanning of single laser pulse. *Opt. Express*, **25**, 28192–28200 (2017). https://doi.org/10.1364/OE.25.028192
47. Damask, J. N. Polarization optics in telecommunications.*Springer*(2004)
48. American National Standard for Safe Use of Lasers (ANSI Z136.1–2000), New York, NY, USA, 2000
49. Bravermay, I. M. The cutaneous microcirculation: ultrastructure and microanatomical organization., **4**, 328–340 (1997). https://doi.org/10.3109/10739689709146797
50. Baran, U., Shi, L. & Wang, R. K. Capillary blood flow imaging within human finger cuticle using optical microangiography. *J. Biophotonics*, **8**, 46–51 (2015).
51. Hu, S. & Wang, L. V. Optical-Resolution Photoacoustic Microscopy: Auscultation of Biological Systems at the Cellular Level. *Biophys J*, **105**, 841–847 (2013). https://doi.org/10.1016/j.bpj.2013.07.017
52. Lin, L. *et al.* Handheld optical-resolution photoacoustic microscopy. *J. Biomed. Opt*, **22**, 041002 (2016). https://doi.org/10.1117/1.JBO.22.4.041002
53. Smith, V. *et al.* Standardisation of nailfold capillaroscopy for the assessment of patients with Raynaud's phenomenon and systemic sclerosis. *Autoimmun Rev*, **19**, 102458 (2020).
54. Levy, B. I. *et al.* Impaired tissue perfusion—a pathology common to hypertension, obesity, and diabetes mellitus., **118**, 968–976 (2008). https://doi.org/10.1161/CIRCULATIONAHA.107.763730
55. Aellen, J. *et al.* Preserved capillary density of dorsal finger skin in treated hypertensive patients with or without type 2 diabetes., **19**, 554–562 (2012). https://doi.org/10.1111/j.1549-8719.2012.00188.x
56. Liu, C., Liang, Y. & Wang, L. Single-shot photoacoustic microscopy of hemoglobin concentration, oxygen saturation, and blood flow in sub-microseconds. *Photoacoustics*, **17**, 100156 (2020). https://doi.org/10.1016/j.pacs.2019.100156

Tables

Table. 1. Comparison of the depth range of the phantom.

	Depth Image		
	Without Distortion Correction	Linear Distortion Correction	Nonlinear Distortion Correction
Max. Depth	591 μm	546 μm	519 μm
Min Depth	336 μm	336 μm	336 μm
Depth Range	255 μm	210 μm	183 μm

Figures

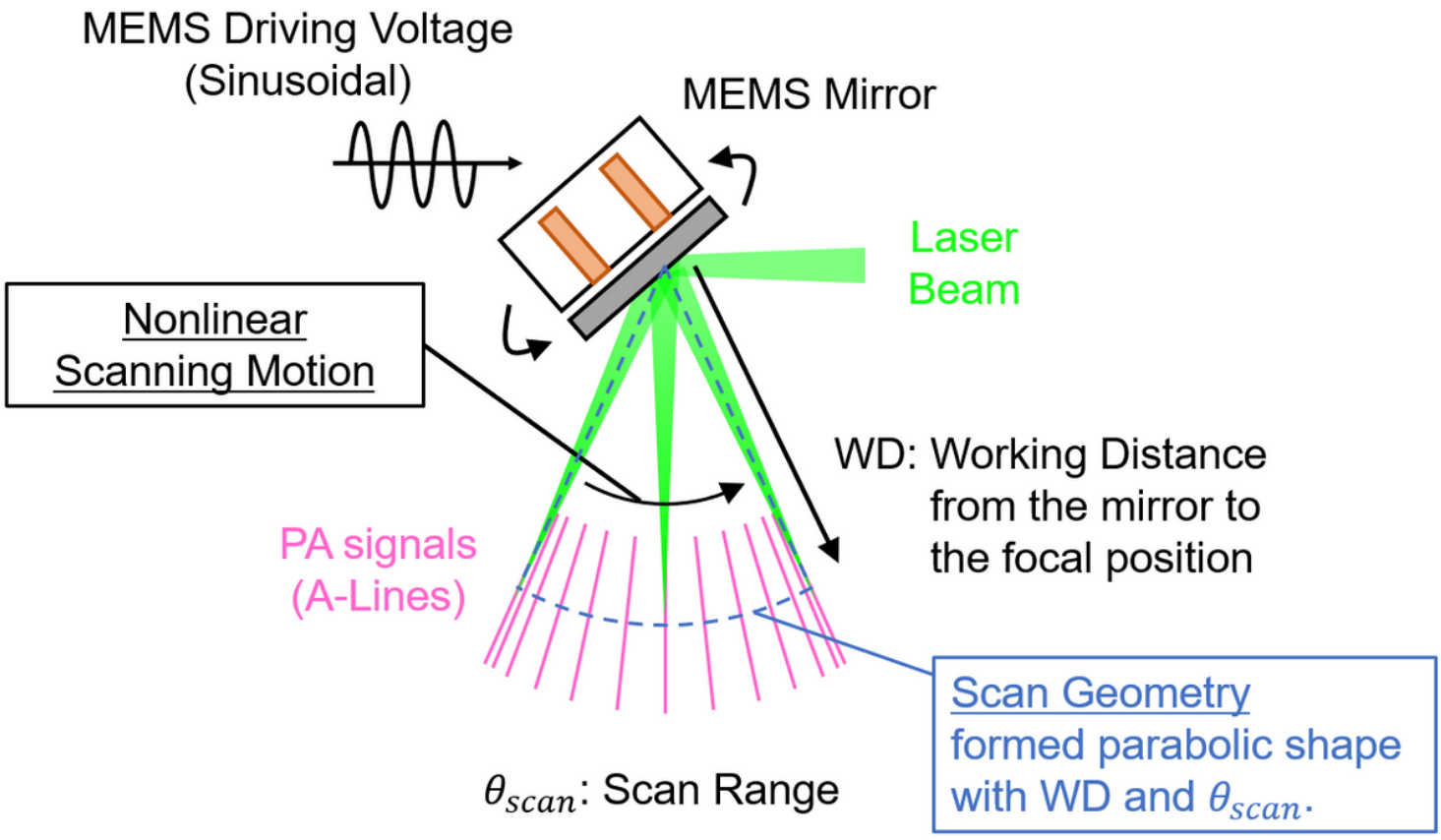

Figure 1

Scan geometry and the nonlinear motion of MEMS scanning mirror.

Figure 2

Schematic of Experimental setup. (a) Block diagram of developed MEMS-OR-PAM system. (b) Photo image. (c) Close-up view of the scanning part.

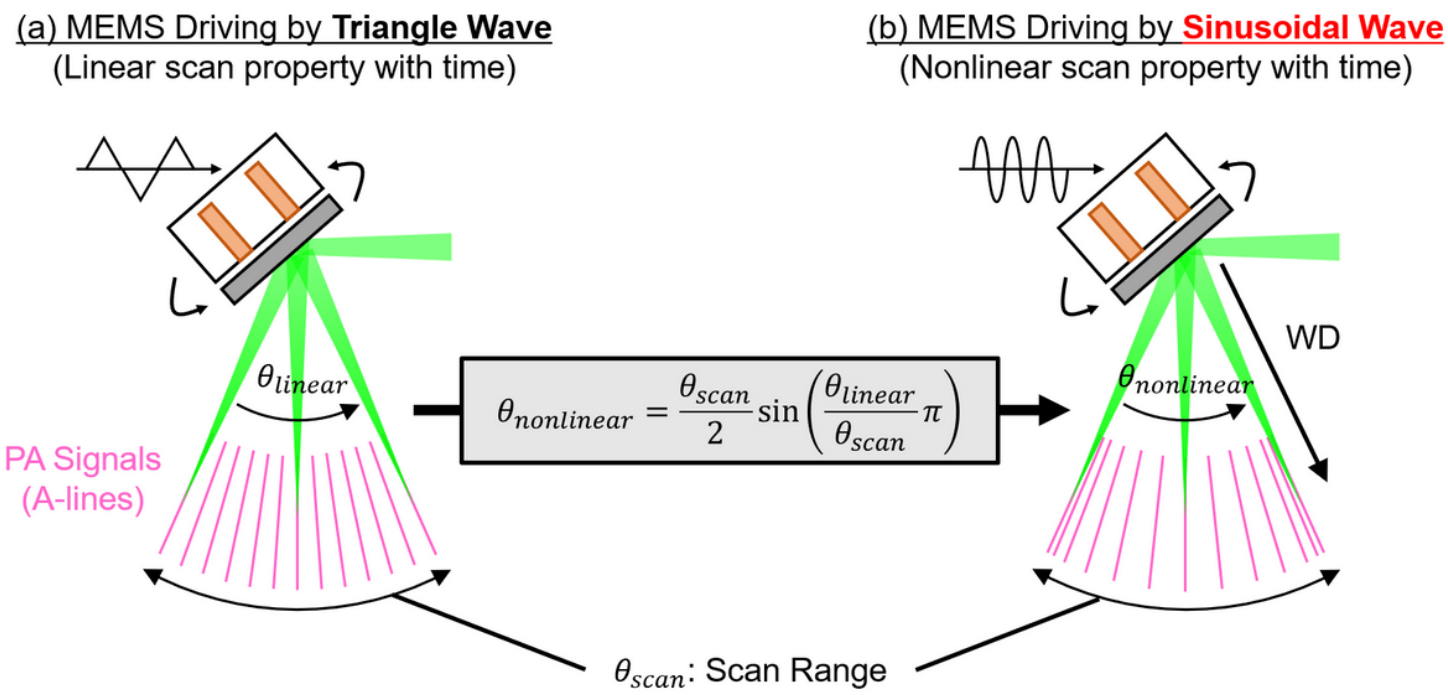

Figure 3

Spatial distortion according to MEMS driving voltage (a) Driving by triangle wave (Linear with the laser PRF timing). (b) Driving by sinusoidal wave (Nonlinear with the laser PRF timing)

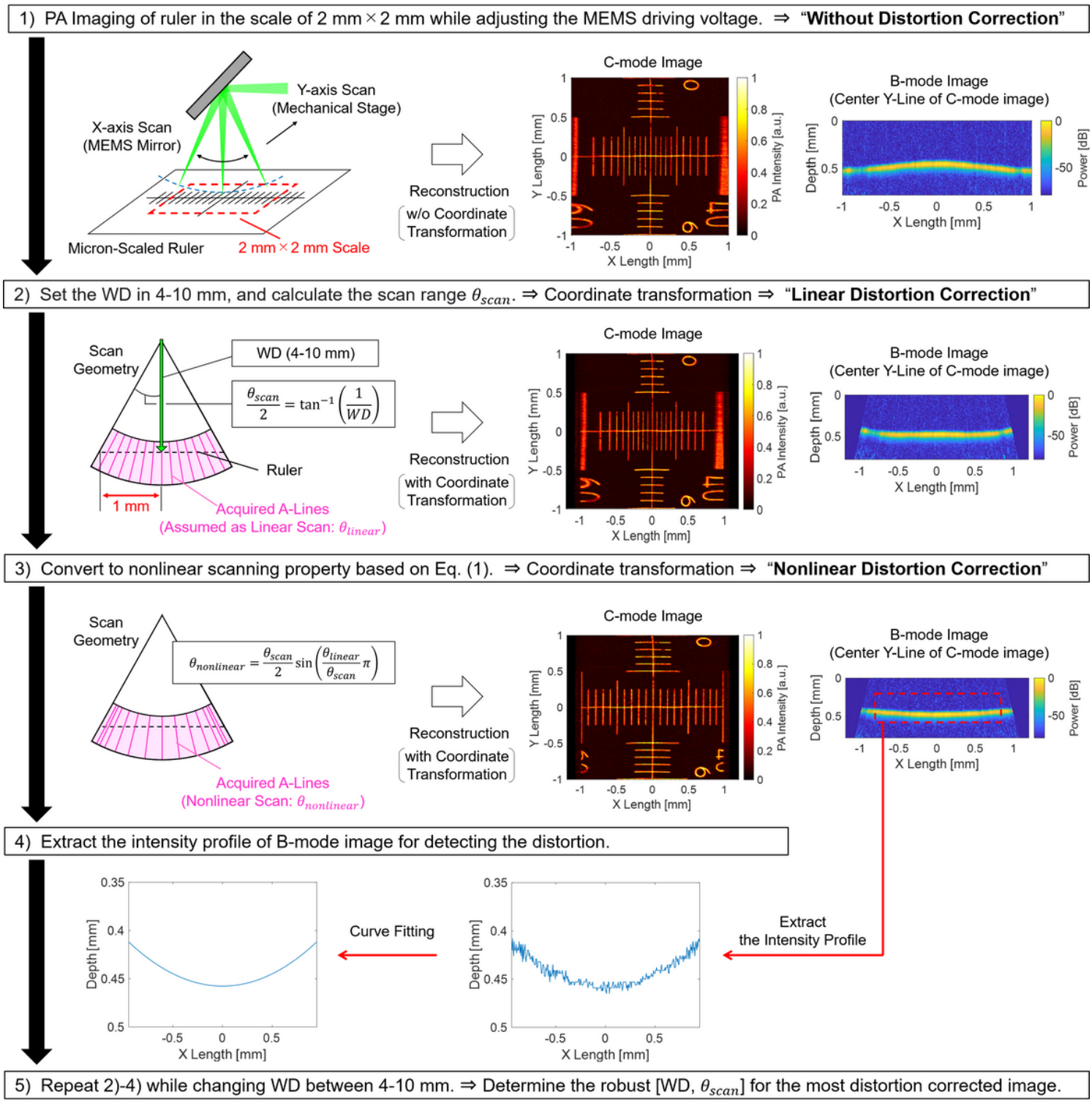

Figure 4

Proposed calibration method for the distortion correction with a ruler.

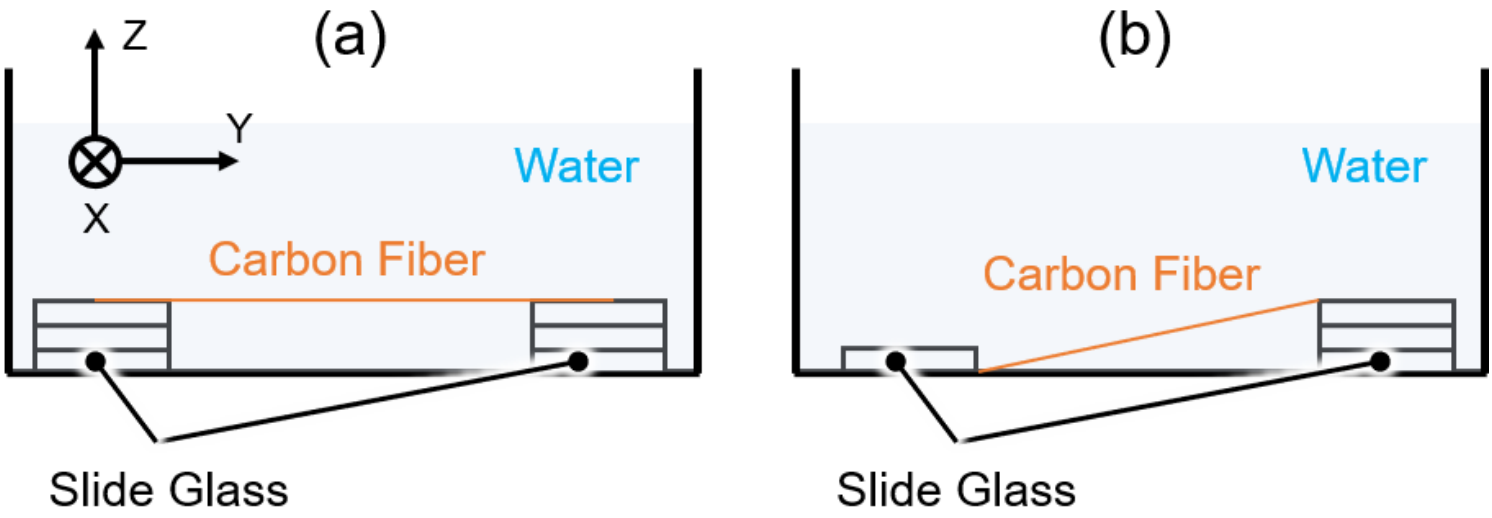

Figure 5

Schematic for carbon fiber preparation. (a) Horizontally stretched for axial resolution measurement. (b) Vertically tilted for DOF measurement.

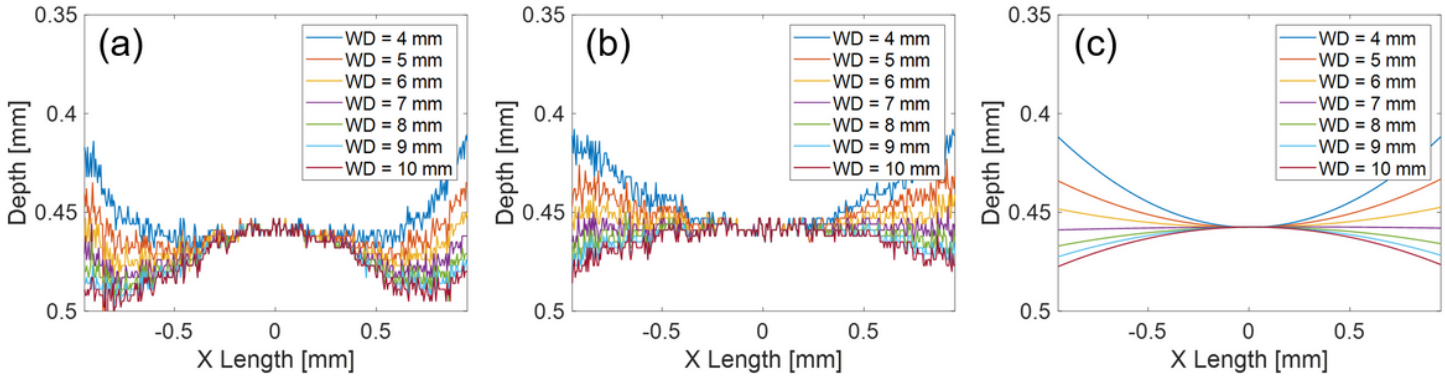

Figure 6

Comparison of the intensity profile extracted from the B-mode image with (a) Linear distortion correction, and (b) Nonlinear distortion correction.

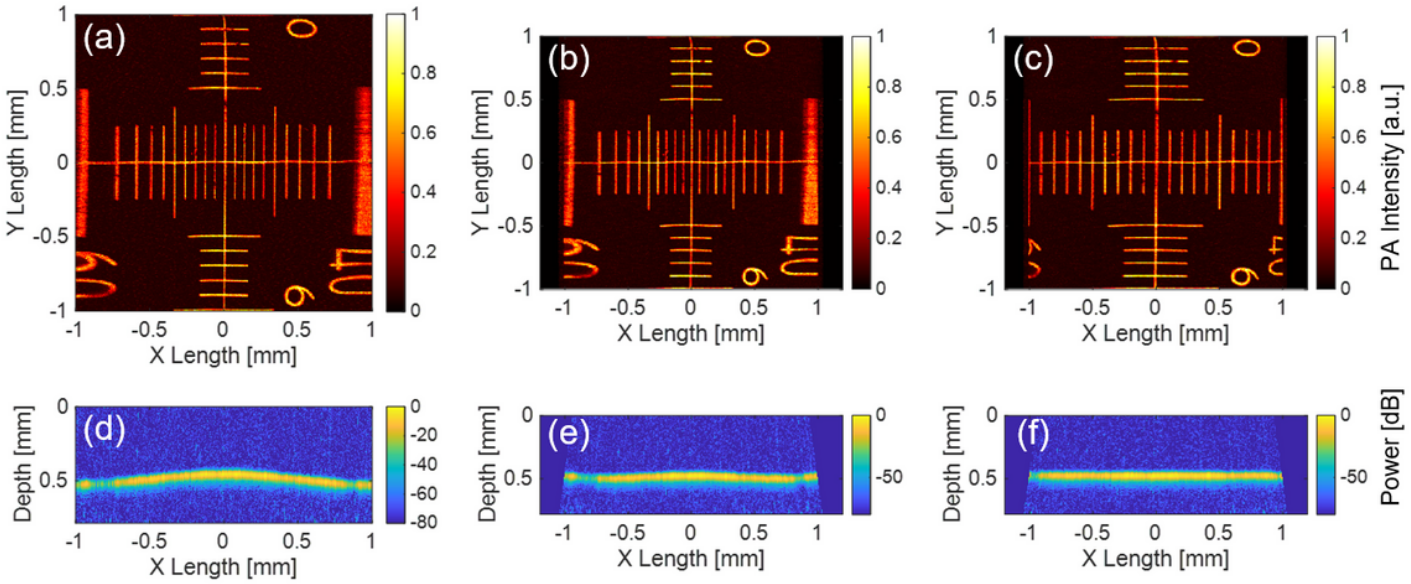

Figure 7

Comparison of C-mode (Upper) and B-mode (Lower, about a center Y-line in C-mode image) images in each distortion correction method. (a, c) Without distortion correction. (b, d) With linear distortion correction (WD=7 mm, θ_scan=16.3 degrees). (c, e) With nonlinear distortion correction (WD=7 mm, θ_scan=16.3 degrees).

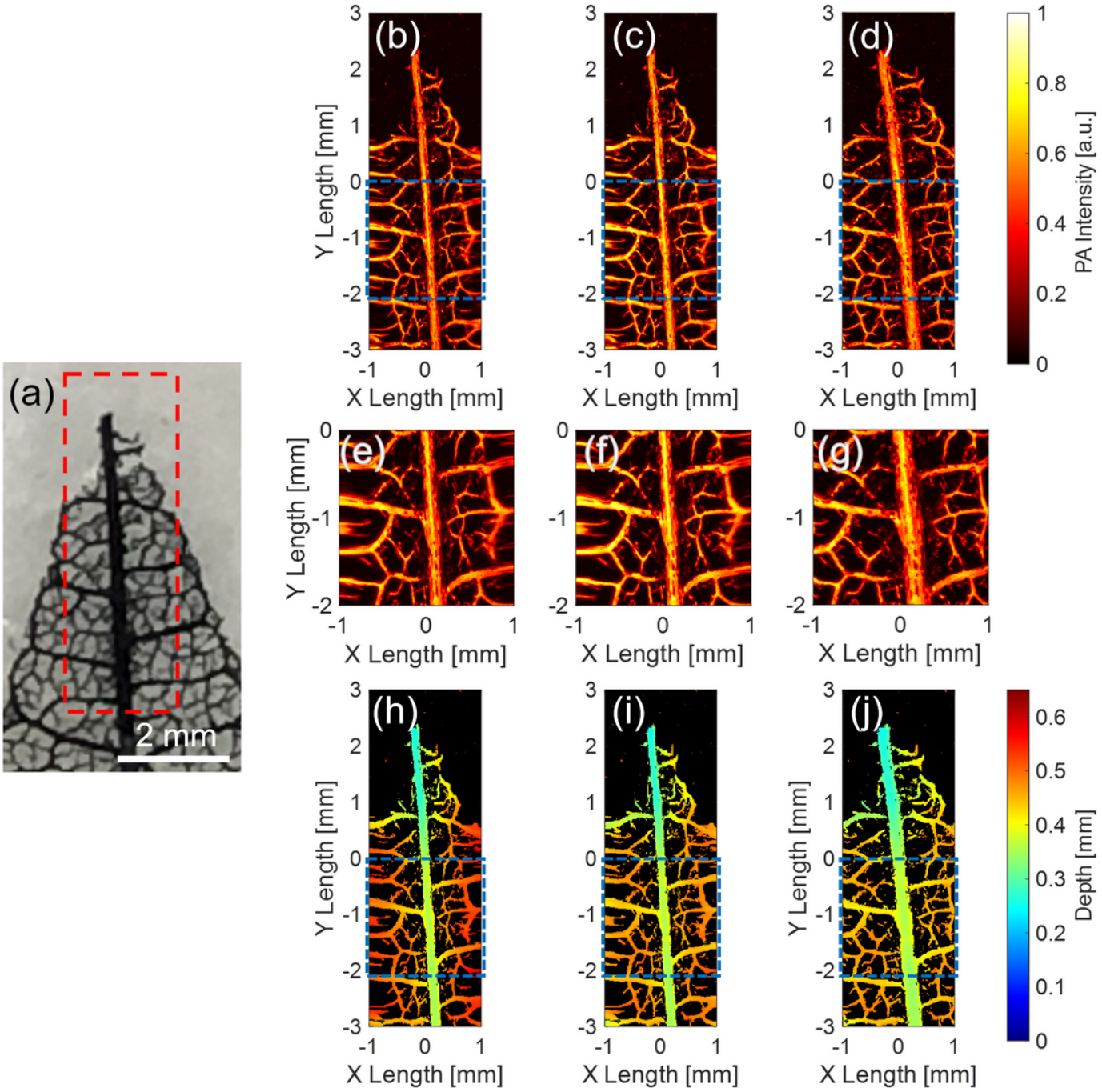

Figure 8

Result of leaf phantom PA imaging with C-mode image (Upper), the enlarged image along the white dotted line (Middle), and the Depth projection image (Lower). (a) Photo image. (b,e,h) PA images without distortion correction. (c,f,i) PA images with linear distortion correction. (d,g,j) PA images with nonlinear distortion correction.

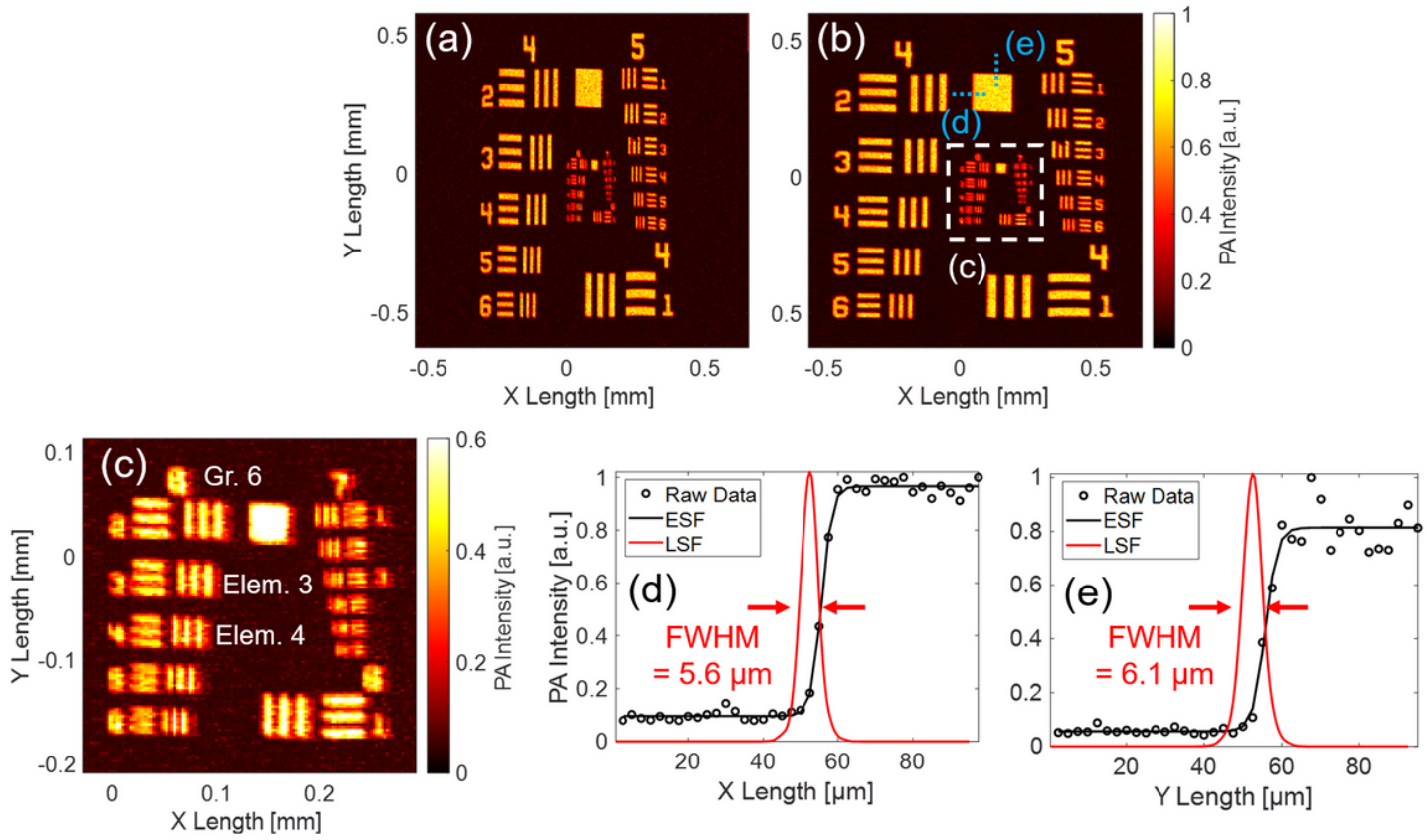

Figure 9

Lateral resolution measurement result with USAF 1951 target. (a) C-mode image without distortion correction. (b) C-mode image with nonlinear distortion correction. (c) Enlarged C-mode image along the white dotted square in (b). (d) Result of LSF method along the X-direction blue dotted line in (c). (e) Result of LSF method along the Y-direction blue dotted line in (d).

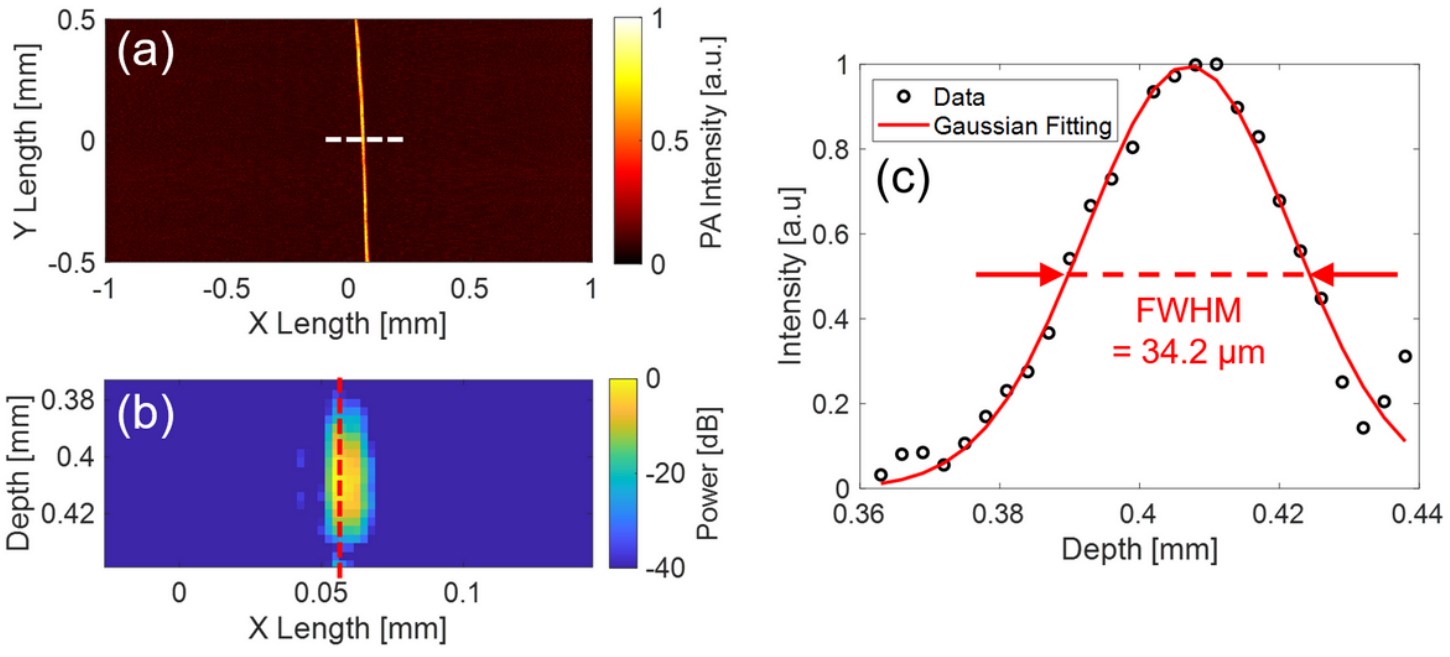

Figure 10

Axial resolution measurement result with a horizontally stretched carbon fiber. (a) C-mode image. (b) B-mode image about the white dotted line in (a). (c) PA envelope profile along the red dotted line in (b) and the Gaussian fitting.

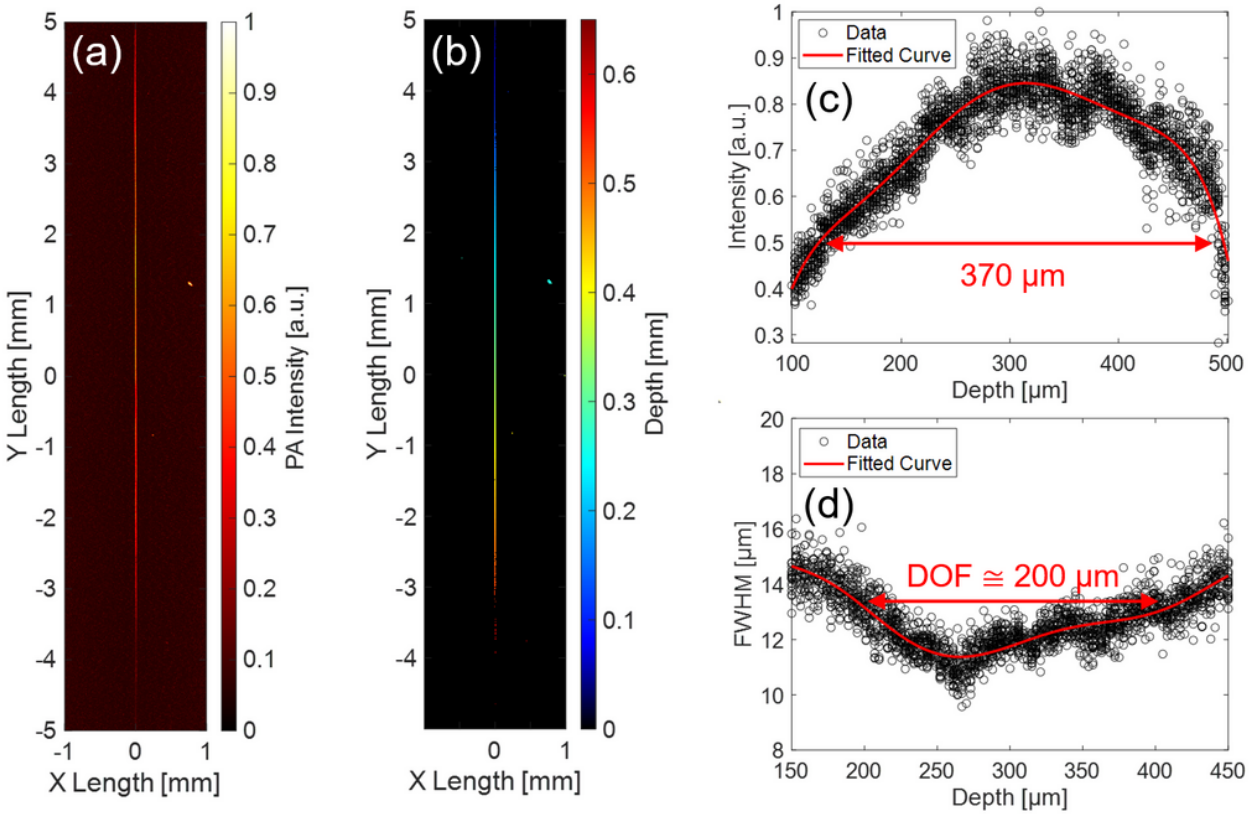

Figure 11

DOF measurement result with a vertically tilted carbon fiber. (a) C-mode image. (b) Depth projection image. (c) PA intensity of the fiber along the depth. (d) FWHM of the fiber along the depth.

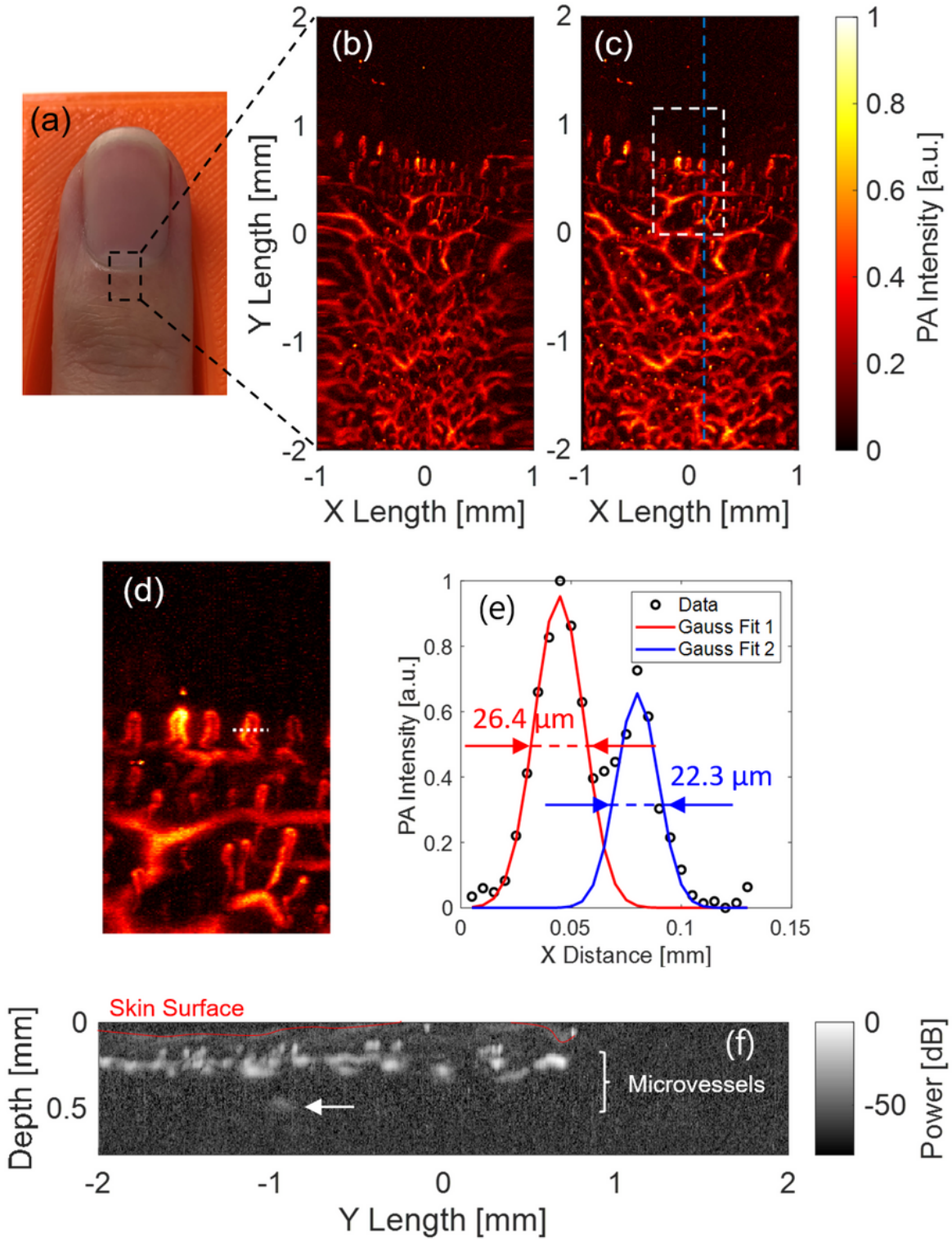

Figure 12

The result of microvascular imaging of human finger. (a) Photo image. (b) C-mode image without distortion correction. (c) C-mode image with linear distortion correction. (d) Enlarged C-mode image along the white dotted square in (c). (e) PA intensity profile along the white dotted line in (d). (f) B-mode image along the blue dotted line in (d).

Supplementary Files

This is a list of supplementary files associated with this preprint. Click to download.

- SupplementaryInformationrevise1115.docx
- SupplementaryMovie.mp4